Moderate heat treatment of CoFe Prussian blue analogues for enhanced oxygen evolution reaction performance

Diao, Fangyuan; Kraglund, Mikkel Rykær; Cao, Huili; Yan, Xiaomei; Liu, Pei; Engelbrekt, Christian; Xiao, Xinxin

Published in:
Journal of Energy Chemistry

Link to article, DOI:
10.1016/j.jechem.2022.11.050

Publication date:
2023

Document Version
Publisher's PDF, also known as Version of record

Journal of Energy Chemistry 78 (2023) 476–486

Contents lists available at ScienceDirect

Journal of Energy Chemistry

journal homepage: www.elsevier.com/locate/jechem

http://www.journals.elsevier.com/journal-of-energy-chemistry/

Moderate heat treatment of CoFe Prussian blue analogues for enhanced oxygen evolution reaction performance

Fangyuan Diao [a], Mikkel Rykær Kraglund [b], Huili Cao [a], Xiaomei Yan [a], Pei Liu [c], Christian Engelbrekt [a,*], Xinxin Xiao [a,d,*]

[a] Department of Chemistry, Technical University of Denmark, Kongens Lyngby DK-2800, Denmark
[b] Department of Energy Storage and Conversion, Technical University of Denmark, Kongens Lyngby DK-2800, Denmark
[c] DTU Nanolab - National Centre for Nano Fabrication and Characterization, Technical University of Denmark, Kongens Lyngby DK-2800, Denmark
[d] Department of Chemistry and Bioscience, Aalborg University, Aalborg 9220, Denmark

ARTICLE INFO

Article history:
Received 17 October 2022
Revised 24 November 2022
Accepted 28 November 2022
Available online 5 December 2022

Keywords:
Prussian blue analogues
PBA derivatives
Oxygen evolution reaction
Electrolyzer

ABSTRACT

Prussian blue analogues (PBAs) with inherent ordered structures and abundant metal ion sites are widely explored as precursors for various electrochemical applications, including oxygen evolution reaction (OER). Using a range of characterization techniques including Fourier-transform infrared spectroscopy (FT-IR), X-ray photoelectron spectroscopy (XPS), X-ray diffraction (XRD) and energy dispersive spectroscopy (EDS), this work discloses the process of replacement of K^+ by NH_4^+ in the interstitial spaces of the CoFe PBA by a hot aqueous urea solution, which influences the transformation of PBAs under further heat treatment and the OER performance of the derivatives. After heat treatment at 400 °C under Ar flow, high-resolution transmission electron microscopy (HRTEM) images reveal that CoFe alloy nanoparticles grew on the crystalline cubes of CoFe PBA with K^+, while CoFe PBA cubes with NH_4^+ become amorphous. Besides, the derivative of CoFe PBA with NH_4^+ (Ar-U-CoFe PBA) performs better than the derivative of CoFe PBA with K^+ (Ar-CoFe PBA) in OER, registering a lower overpotential of 305 mV at 10 mA cm^{-2}, a smaller Tafel slope of 36.1 mV dec^{-1}, and better stability over a testing course of 20 h in 1.0 M KOH. A single-cell alkaline electrolyzer, using Ar-U-CoFe PBA and Pt/C for the anodic and cathodic catalyst, respectively, requires an initial cell voltage of 1.66 V to achieve 100 mA cm^{-2} at 80 °C, with negligible degradation after 100 h.

1. Introduction

Prussian blue analogues (PBAs) represent a family of metal-cyanide frameworks sharing a chemical formula $A_xM[M'(CN)_6]_{1-y}\gamma_y{\cdot}nH_2O$ (where A represents alkali metal ions such as Na^+ and K^+, M and M' correspond to different transition metals (e.g., Fe, Co, Ni, and Cu), and γ represents the $[M'(CN)_6]$ vacancy) [1,2]. These materials can refer to MM' PBAs. The rich metal variety with a wide range of ratios of metal elements enables a large PBA family, featuring a series of properties and applications [3]. For example, CoFe PBAs with a face-centred cubic structure show photomagnetic effects, which are sensitive to the species of alkali metal ions [4,5]. PBAs are widely reported cathodic materials of secondary batteries which employ alkali metal ions (e.g., Li^+, Na^+, and K^+), alkaline earth metal ions, and other multivalent ions (e.g., Mg^{2+}, Ca^{2+}, Zn^{2+}, and Al^{3+}), because their open channels and interstitial space (3.2 Å in diameter for the open ⟨100⟩ channels; 4.6 Å in diameter for the interstitial space) constructed by M'–C≡N–M are large enough for the insertion/de-insertion of cations [3,6]. Some small ions or molecules can also be accommodated in the interstitial space of PBAs. For instance, PBAs are good candidates for ammonium-ion aqueous rechargeable batteries, attracting growing attention for large-scale electricity storage due to their advantages of low cost and high safety [7,8]. Prussian blue (PB) and PBAs behave well in gas absorption applications with gases like H_2, CO_2, and NH_3 [9–12]. Takahashi et al. found that PB and PBAs (CoCo PBA and CuFe PBA) can capture ammonia in ambient air at interstitial and vacancy sites, and the absorbed ammonia prefers to transform into NH_4^+ in the presence of H_2O with prolonged exposure time [12]. The above literature highlights that the alkali metal ions in PBAs can be exchanged with other cations.

* Corresponding authors.
E-mail addresses: cheng@kemi.dtu.dk (C. Engelbrekt), xixiao@kemi.dtu.dk (X. Xiao).

https://doi.org/10.1016/j.jechem.2022.11.050
2095-4956/

PBAs and their derivatives are also promising candidates for oxygen evolution reaction (OER) catalysts, featuring low-cost, simple synthesis, ease of scale-up, adjustable metal species, etc. [13,14]. Lee and coworkers used $Na_xM[Fe(CN)_6]_{1-y}\ \gamma_y{\cdot}nH_2O$ (MFe PBA, M = V, Fe, Co, and Ni) as platform materials to compare their OER activities, with NiFe PBA showing the highest current density of 59 mA cm^{-2} at a working potential of 1.7 V, but only 3.2 mA cm^{-2} for VFe PBA. The authors attributed such an OER activity difference to the distinctive binding energy difference between *O and *OH on their surfaces [15]. Han et al. studied the OER performance of $Co_4(Fe(CN)_6)_{2.67}{\cdot}(H_2O)_{15.33}$ growing on fluorine-doped tin oxide (FTO) coated glass in a wide pH range, which shows excellent activity, stability, and corrosion resistance even in strong acidic condition (pH = 2) [16]. Heat treatment is a versatile method to fabricate PBA derivatives including metal oxides, metal sulfides, metal phosphides, and alloys by adjusting the atmosphere, temperature, and other experimental parameters. It can also introduce defects to PBAs. For example, Zeng et al. reported a heat treatment method with an additional salt-encapsulation pre-step, which converted NiFe PBA cubes into a composite of nanoparticle-connected NiFe PBA, amorphous carbon, and metal oxides, exposing more active sites for OER performance. The sample prepared at 400 °C, requiring an overpotential of 285 mV at 50 mA cm^{-2} and showing a Tafel slope of 53.1 mV dec^{-1}, which outperformed that of RuO_2 [17]. PBAs can also be transformed into metal nitrides in the co-atmosphere of N_2 and NH_3 flow at 450 °C [18,19]. Kwag et al. successfully synthesized nanocrystalline Fe_2Ni_2N/rGO nanohybrid sheets through ammonolysis of NiFe PBA/rGO precursors [18]. Kang et al. prepared mesoporous Co_3N@amorphous N-doped carbon nanocubes, exhibiting a low Tafel plot of 69.6 mV dec^{-1} and a low overpotential of 280 mV at 10 mA cm^{-2} [19]. However, the role of the species in the interstitial space in PBAs' structural and compositional evolution during heat treatment, as well as their corresponding influence on derivatives' OER performance, has received little attention.

In this contribution, we have prepared four samples including CoFe PBA synthesized via a facile co-precipitation method, the urea-treated CoFe PBA (U-CoFe PBA), heat-treated CoFe PBA (Ar-CoFe PBA), and heat-treated U-CoFe PBA (Ar-U-CoFe PBA) (Scheme 1). Through comprehensive characterization, it is found that a hydrothermal step with an aqueous urea solution can effectively replace K^+ in the interstitial space of CoFe PBA with NH_4^+. This exchange leads to the completely different behaviours of the heat-treated derivatives and the corresponding OER performance. Ar-CoFe PBA and Ar-U-CoFe PBA show superior activity to their precursors, with Ar-U-CoFe PBA showing higher stability over Ar-CoFe PBA.

2. Methods

2.1. Chemicals and materials

All chemicals were used as received without further purification unless otherwise mentioned. Sodium citrate dihydrate ($Na_3C_6H_5O_7{\cdot}2H_2O$, ≥99%), cobalt (II) nitrate hexahydrate ($Co(NO_3)_2{\cdot}6H_2O$, ≥98%), urea (NH_2CONH_2, ≥99.0%), potassium hexacyanoferrate (III) ($K_3[Fe(CN)_6]$, ≥99%), 2-propanol ($(CH_3)_2CHOH$, anhydrous, ≥99.5%), hydrochloric acid (HCl, 37 wt%, 1.2 g mL^{-1} at 25 °C), and Nafion™ perfluorinated ion-exchange resin (10 wt% in H_2O) were purchased from Sigma-Aldrich. Ethanol absolute (≥99.5%) was provided by VWR Chemical BDH. Carbon black (75 $m^2\ g^{-1}$, ≥99.9%) and 10 wt% platinum on carbon black (Pt/C) were bought from Alfa Aesar. 1.0 M potassium hydroxide (KOH, pH = 14) solution was purchased from Fisher Chemical. Aemion+™ High IEC membrane (AF2-HLE8-40-X, thickness: 40 μm) was supplied by

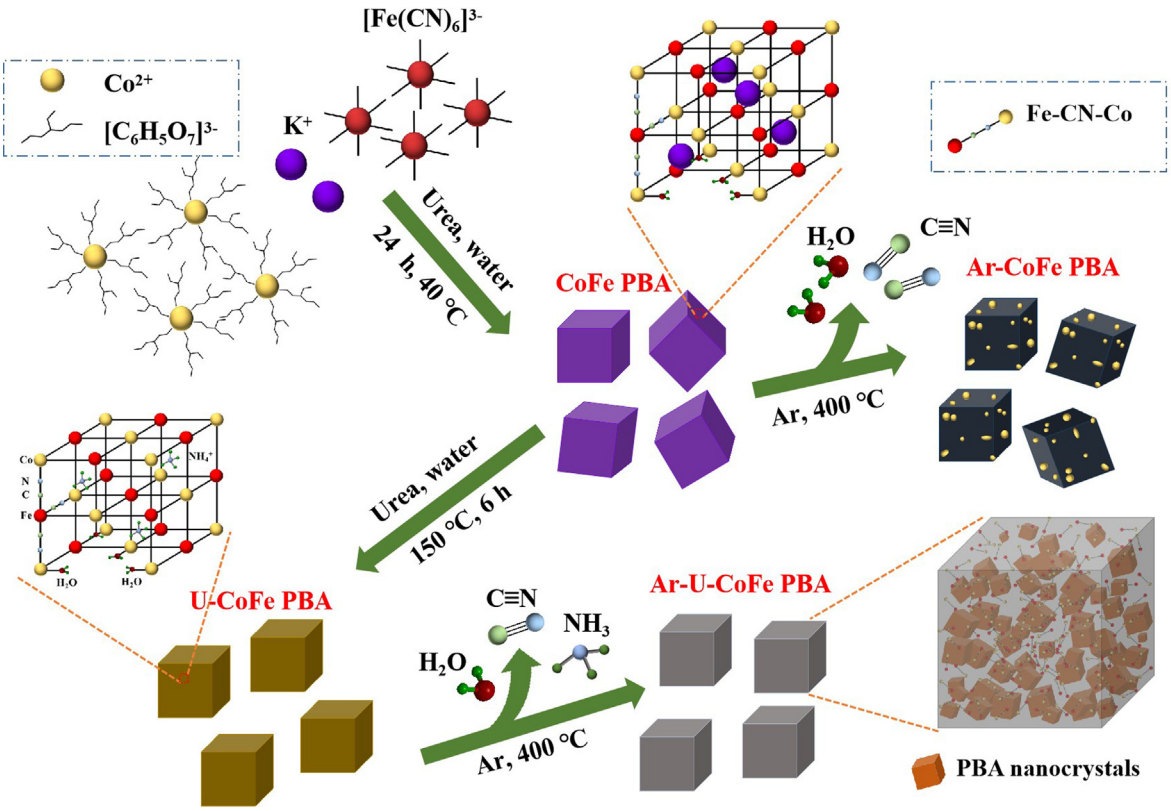

Scheme 1. Synthesis route. Schematic illustration of the synthesis route for CoFe PBA, U-CoFe PBA, Ar-CoFe PBA, and Ar-U-CoFe PBA.

Ionomr Innovations, which was immersed in 1.0 M KOH for 24 h before usage. Aemion+™ High IEC ionomer (AP2-HNN8-00-X, Ionomr Innovations) was received in powder. Ni foam (thickness: 300 μm) was purchased from Suzhou Jiashide Metal Foam Co., ltd., China, which was cleaned with ethanol, 1.0 M HCl solution, and water successively before usage. Ultrapure water was prepared with Arium® Pro VF Ultrapure Water System (Sartorius AG, Germany, 18.2 MΩ cm).

2.2. Preparation of CoFe PBA, U-CoFe PBA, and their derivatives

(i) Preparation of CoFe PBA. CoFe PBA cubes were synthesized by a facile co-precipitation method [20]. 100 mL aqueous solution with 2.0 mmol $K_3[Fe(CN)_6]$ was slowly poured into 100 mL aqueous solution containing 3.0 mmol $Co(NO_3)_2{\cdot}6H_2O$ and 4.5 mmol $Na_3C_6H_5O_7{\cdot}2H_2O$ under stirring. The obtained solution was stirred for another 20 min and then aged in an oven at 40 °C for 24 h. Finally, the precipitate was collected via centrifugation, washed with water three times, and dried in a vacuum oven at 80 °C for 24 h.

(ii) Preparation of U-CoFe PBA. 0.300 g CoFe PBA was dispersed in a 90 mL aqueous solution containing 0.901 g urea. The mixed solution was sonicated for at least 20 min and transferred to a 150 mL Teflon-lined autoclave and treated at 150 °C for 6 h. After the autoclave cooled naturally down to the room temperature, the U-CoFe PBA powder was collected and washed with water three times by centrifugation. The sample was finally dried in a vacuum oven at 80 °C for 24 h.

(iii) Heat-treatment of CoFe PBA and U-CoFe PBA. Obtained CoFe PBA and U-CoFe PBA were treated in a tube furnace at 400 °C for 2 h with a heating rate of 2 °C min^{-1} under an Ar atmosphere. After natural cooling to room temperature, samples were collected and labelled as Ar-CoFe PBA and Ar-U-CoFe PBA, respectively. Control samples treated at other temperatures (200, 300, and 600 °C) were named as Ar-CoFe PBA T °C and Ar-U-CoFe PBA T °C, respectively, where T represents the heat treatment temperature.

2.3. Characterization methods

Powder X-ray diffraction (XRD) patterns were acquired with a Huber G670 Guinier camera using Cu $K_{\alpha 1}$ radiation (λ = 1.54056 Å) with 40 kV and 40 mA. X-ray photoelectron spectroscopy (XPS) results were collected on a Thermo Fisher Scientific Nexsa XPS system. Fourier transform infrared (FT-IR) spectra were collected on a Bruker Alpha-P FT-IR spectrophotometer. The material morphology was characterized with a scanning electron microscope (SEM, FEI Quanta FEG 250 Analytical ESEM). Transmission electron microscopy (TEM) images, high-resolution TEM (HRTEM) images, and the corresponding energy dispersive spectroscopy (EDS) analysis were collected with a Tecnai T20 G2 at 200 kV equipped with a TVIPS XF416 4 k × 4 k camera. Thermal gravimetric analysis (TGA) was measured at a heating rate of 2 °C min^{-1} in N_2 and heated up to 700 °C on a thermogravimetric analyzer (Mettler Toledo). The specific surface area was measured using nitrogen adsorption at 77 K by the Brunauer-Emmett-Teller (BET) method with a Micromeritics ASAP 2020.

2.4. Electrochemical measurements

Primary electrochemical tests were carried out in a three-electrode cell containing O_2-saturated 1.0 M KOH at room temperature on a CHI 760C electrochemical workstation (CH Instruments, Inc. USA), or an Autolab potentiostat (Eco Chemie, the Netherlands). A carbon rod and a Hg/HgO (1.0 M KOH) electrode were used as the counter and reference electrodes, respectively. All potentials were calibrated to the reversible hydrogen electrode (RHE) ($E_{vs.\ RHE} = E_{vs.\ Hg/HgO}$ + 0.098 + 0.059 pH). The catalyst ink was prepared by dispersing 4.0 mg of the sample and 2.0 mg of carbon black in a mixture of 25 μL Nafion solution, 250 μL water, and 750 μL 2-propanol. After ultrasonication for 1 h, 10 μL of the prepared ink was drop-cast onto the polished rotating disk glassy carbon electrode (RDE, disk area: 0.1963 cm^2) and dried in the air, leading to a final catalyst loading of ~0.20 mg cm^{-2}. Linear sweep voltammetry (LSV) and cyclic voltammetry (CV) curves without *i*R compensation were collected at a scan rate of 5 mV s^{-1} after curves have been stabilized. LSV and CV curves are presented as collected without *i*R compensation unless specified. The overpotential (η) at a specific current density (i) is calculated by the equation: $\eta = E(i) - 1.23$ V, where $E(i)$ represents the potential at the current density of i in mA cm^{-2}. Electrochemical impedance spectroscopy (EIS) measurements were carried out at 1.60 V in a frequency range of 10 kHz – 0.01 Hz, with an amplitude of 5 mV.

The operational stability of OER was preliminarily studied with the chronopotentiometry (CP) method at 10 mA cm^{-2} for 20 h on RDE at 1600 r min^{-1} to remove generated gas bubbles. Ar-CoFe PBA and Ar-U-CoFe PBA were also pasted on the Ni foam (mass loading: 2.0 mg cm^{-2}, without the addition of carbon black) for a 40 h CP test at 10 mA cm^{-2} in 1.0 M KOH at room temperature. The samples after stability test were dried in vacuum for further XPS and TEM analysis.

A two-electrode water electrolysis test was performed in a single-cell alkaline electrolyzer. 1.0 M aqueous KOH solution was circulated throughout the cell at a flow rate of 80 mL min^{-1}. The electrolyte temperature was controlled by heating elements and thermocouples in the flow-field plates. The Aemion + membrane was used as the separator. Ar-U-CoFe PBA (~8.6 mg cm^{-2}) and Pt/C (~3.7 mg cm^{-2}) were sprayed on Ni foam by airbrushing, and employed as the anode and cathode, respectively. Specifically, the catalyst ink was prepared by adding 0.04 g catalyst into a mixed solution of 1.40 g 2-propanol and 1.00 g 1 wt% ionomer solution (volume ratio of ethanol: H_2O = 1:1) under sonication at room temperature to obtain a homogenous ink. The total solid content (catalyst and ionomer, with a weight ratio of 4:1) in the catalysts ink was 2.05 wt%. During spraying, Ni foam was placed on a hotplate at 120 °C. Polarization curves at various operational temperatures of 40, 60, and 80 °C, alongside CP curve at 100 mA cm^{-2} and 80 °C over a time course of 100 h, were obtained.

3. Results and discussion

3.1. Synthesis method and structural characterization

3.1.1. CoFe PBA

CoFe PBA, U-CoFe PBA, and their derivatives are fabricated following the route as illustrated in Scheme 1. CoFe PBA is synthesized via a co-precipitation method where Co^{2+} and $[Fe(CN)_6]^{3+}$ in the solution react to form the CoFe PBA precipitate. During this process, citrate ions are also involved by coordinating with Co^{2+}, posing control over the nucleation and crystal growth [20]. After the reaction, a deep purple precipitate is collected by centrifugation, displaying a uniformly cubic morphology (side length: 127 ± 9 nm) and smooth surfaces as confirmed by SEM and TEM (Fig. S1a and Fig. 1a). The selected area electron diffraction (SAED) pattern (Fig. 1b) of an ensemble of CoFe PBA cubes shows a polycrystalline feature, with circles from the inside to the outside that are attributed to the plane (2 0 0), (2 2 0), and (4 0 0), respectively. These planes are in accordance with peaks at 17.6°, 25.1°, and 35.7° of the corresponding XRD pattern (Fig. 2a) (Inorganic Crystal Structure Database (ICSD) Collection Code: 164830) [21]. The lattice parameter of CoFe PBA is calculated to be 10.06 Å from the XRD

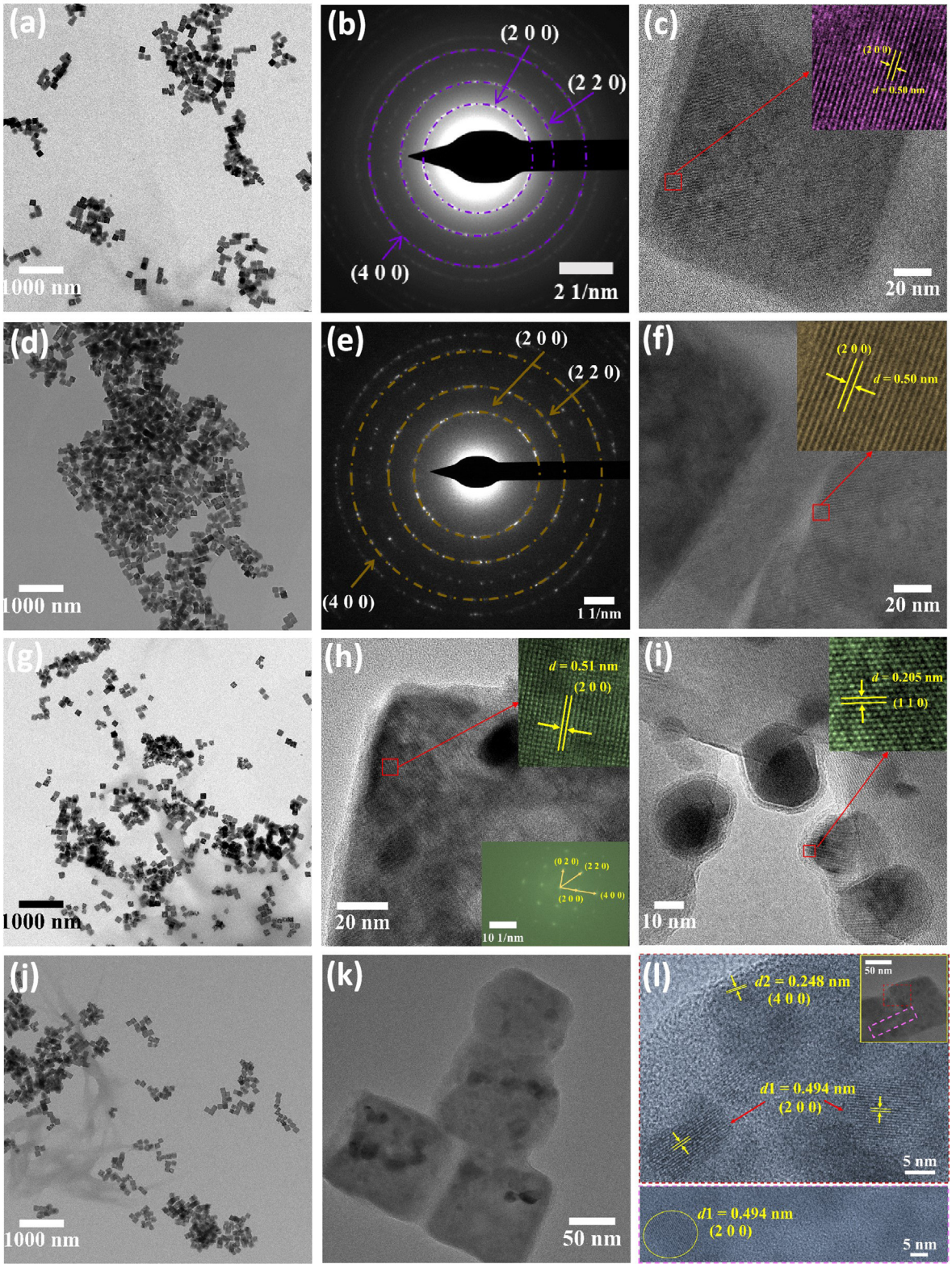

Fig. 1. Morphology characterization of the samples. TEM images, SAED patterns, and HRTEM images of CoFe PBA (a–c) and U-CoFe PBA (d–f). TEM image (g), HRTEM image and the corresponding FFT pattern of the lattice on the cube (h), and HRTEM image of the nanoparticle on the surface (i) of Ar-CoFe PBA. TEM images (j, k) and the magnified HRTEM images (l) of Ar-U-CoFe PBA. Insets of (c, f, h, and i) are the magnified HRTEM images of the corresponding samples.

pattern, consistent with the lattice fringe spacing measured from the HRTEM image (Fig. 1c). With the assistance of EDS (Fig. S2), the final formula of CoFe PBA is determined to be $K_{1.1}Co[Fe(CN)_6]_{0.8}\gamma_{0.2}\cdot nH_2O$. Chemical bonds in CoFe PBA are further examined by FT-IR (Fig. 2b). Broad bands at around 3387 and 1608 cm^{-1} correspond to the O—H stretching mode and H—O—H bending vibration from water, respectively [22]. The band at 3624 cm^{-1} can be explained by the –OH stretching mode in

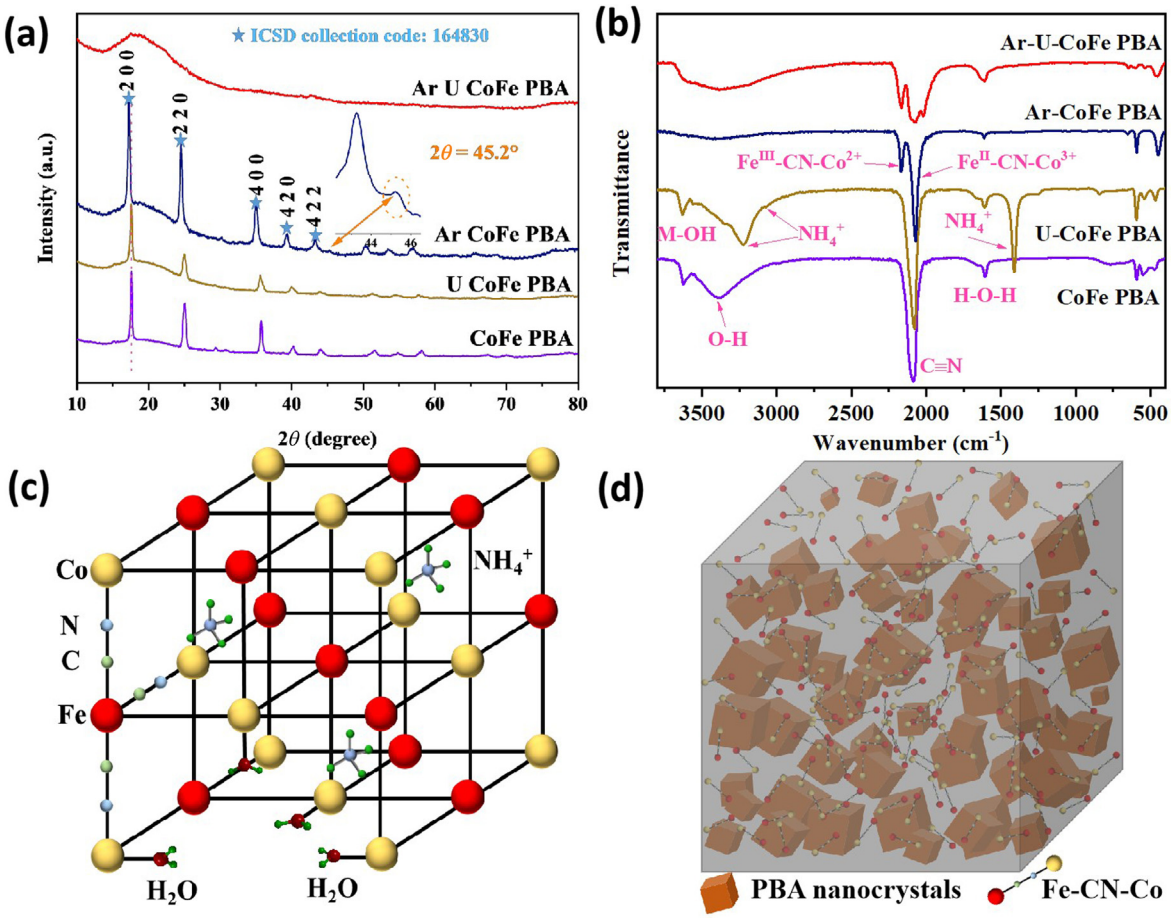

Fig. 2. Compositional characterization and structural illustration. XRD patterns (a), and FT-IR spectra (b) of CoFe PBA, U-CoFe PBA, Ar-CoFe PBA, and Ar-U-CoFe PBA. Inset of (a) is the magnified image of the peak around 45.2 degree of the XRD pattern of Ar-CoFe PBA. Illustrated crystal structure of U-CoFe PBA (c) and illustrated composition of Ar-U-CoFe PBA (d).

Metal-OH (Metal refers to Co and Fe in CoFe PBA, –OH is from absorbed H_2O) [23,24]. This observation further confirms the presence of water molecules in CoFe PBA. The band at 2087 cm^{-1} is assigned to the stretching vibration of the CN groups in Fe-CN-Co units. In the far-IR region, two bands appear at 592 and 471 cm^{-1}, representing Fe-CN and Co-CN flexural vibration absorption, respectively [25].

3.1.2. U-CoFe PBA

U-CoFe PBA, a brown powder, is obtained by the hydrothermal treatment of CoFe PBA in an aqueous urea solution at 150 °C. Such a hydrothermal procedure retains the cubic shape of the pristine PBA with a similar particle size (130 ± 9 nm) and smooth surfaces, as indicated by SEM and TEM images (Fig. S1b and Fig. 1d). Based on the sample powder XRD pattern and SAED pattern (Fig. 2a and Fig. 1e), U-CoFe PBA also shares the same crystalline characteristics as CoFe PBA. Notably, XRD peaks of U-CoFe PBA shift to a smaller angle in comparison with CoFe PBA, relative to the expansion of its cell parameter (a = 10.07 Å). As shown in Fig. 1(f), the HRTEM image of the U-CoFe PBA cube further demonstrates its crystalline structure. The atomic ratio of Co to Fe in U-CoFe PBA (Co:Fe = 1:0.8) obtained by EDS analysis is identical to that of CoFe PBA (Figs. S2 and S3). Differences between U-CoFe PBA and the pristine CoFe PBA are further revealed by EDS, XPS and FT-IR spectra. In comparison to the EDS spectrum of CoFe PBA, U-CoFe PBA finds the disappearance of K, which is further validated by the XPS spectra (Fig. S4a). Furthermore, a new peak at around 1412 cm^{-1} appears in the FT-IR spectrum of U-CoFe PBA (Fig. 2b), suggesting that the hydrothermal process introduces new species into U-CoFe PBA to maintain the overall charge neutrality.

During the hydrothermal process at 150 °C, urea reacts with water, producing CO_2 and NH_3 (Eq. (1)). NH_3 combines with H_2O to form $NH_3{\cdot}H_2O$, which dissociates in water to form NH_4^+ and OH^- (Eq. (2)).

$$CO(NH_2)_2 + H_2O \rightarrow CO_2 + 2NH_3 \quad (1)$$

$$NH_3 + H_2O \rightarrow NH_3{\cdot}H_2O \leftrightarrow NH_4^+ + OH^- \quad (2)$$

Ultimately, NH_4^+ in the solution replaces K^+ in the interstitial space of CoFe PBA. NH_4^+ is also likely to replace partial zeolitic water molecules as U-CoFe PBA registers a smaller weight loss by 3.3 wt% around 150 °C than that of CoFe PBA on their TGA curves (Fig. S5) [26,27]. The characteristic FT-IR peaks of urea are mainly located at 1400–1700 cm^{-1}, including the peak of C=O at about 1675 cm^{-1}, and C—N at about 1455 cm^{-1} (Fig. S6), quite different from that of U-CoFe PBA [28,29]. They are not observed in the FT-IR spectrum of U-CoFe PBA. Instead, new bands located at around 3220 and 1412 cm^{-1} are assigned to triply degenerate stretching vibration and bending vibration of NH_4^+, respectively, indicating the incorporation of NH_4^+ in the U-CoFe PBA structure [12,30–33]. In the N 1s XPS spectra of CoFe PBA (Fig. S4b), a new peak around 402.5 eV corresponding to NH_4^+ further supports this speculation [34,35]. The proposed structure of U-CoFe PBA is illus-

trated in Fig. 2(c). The formula of U-CoFe PBA is estimated to be $(NH_4)_{1.9}Co[Fe(CN)_6]_{0.8}\gamma_{0.2}\cdot mH_2O$ based on the elemental analysis by EDS (Fig. S3).

3.1.3. Ar-CoFe PBA

Two derivatives, Ar-CoFe PBA and Ar-U-CoFe PBA, are obtained by the heat treatment of CoFe PBA and U-CoFe PBA under Ar flow at 400 °C for 2 h, respectively. Ar-CoFe PBA maintains the cubic morphology as examined by SEM and TEM (Fig. S1c and Fig. 1g). Nanoparticles of approximately 20 nm in diameter, can be found on the surface of Ar-CoFe PBA cubes by TEM (Fig. 1i and Fig. S7). The HRTEM image of Ar-CoFe PBA (Fig. 1h) exhibits a clear lattice fringe with a spacing of 0.51 nm, corresponding to the (2 0 0) plane of CoFe PBA crystal. The associated fast Fourier transform (FFT) pattern (inset of Fig. 1h) indicates the angular relationships of different planes, which are also in agreement with the cubic crystal structure. Major peaks on the XRD pattern of Ar-CoFe PBA (Fig. 2a) are consistent with CoFe PBA, with a tiny decrease of 2θ, representing a larger cell parameter (a = 10.25 Å). These results indicate that the cubes of Ar-CoFe PBA maintain the PBA feature after heat treatment. The HRTEM image of the nanoparticle on the cube (inset of Fig. 1i) shows lattice fringes spacing of about 0.205 nm. The corresponding EDS (Figs. S7b and c) shows the present Co and Fe (no K and N), and a higher Co/Fe atomic ratio than CoFe PBA. Besides, the XRD pattern of Ar-CoFe PBA witnesses the appearance of a new peak at around 45.2° compared to CoFe PBA, which is in accordance with the plane (1 1 0) of CoFe alloy (ICSD Coll. Code of 102381) [17]. Therefore, it can be deduced that Co and Fe atoms combine to form CoFe alloy nanoparticles after losing CN ligands during heat treatment. The FT-IR spectrum of Ar-CoFe PBA (Fig. 2b) registers the disappearance of broad bands in the range of 3700–3000 cm^{-1} of CoFe PBA, suggesting the loss of water molecules. Two bands at around 2072 and 2169 cm^{-1} correspond to the stretching of CN ligands in the Fe^{II}-CN-Co and Fe^{III}-CN-Co, respectively [25,36,37]. Based on the above analysis, the heat treatment process at 400 °C is believed to effectively remove water molecules, and a part of CN groups in CoFe PBA, resulting in under-coordinated Co and Fe forming CoFe alloy nanoparticles.

3.1.4. Ar-U-CoFe PBA

TEM image of Ar-U-CoFe PBA (Fig. 1j) shows the maintained cubic morphology, with an average particle size of 117 ± 9 nm. Nanoparticle-like dark spots form and disperse in cubes after heat treatment (Fig. 1k). Besides this, atoms in some areas of the cube are disordered under HRTEM with a few of areas (diameter: ≤15 nm) displaying clear lattice fringes as shown in Fig. 1(l), which is different from U-CoFe PBA. XRD pattern of Ar-U-CoFe PBA (Fig. 2a) also shows an amorphous feature, without evident peaks. Therefore, it can be concluded that Ar-U-CoFe PBA consists of a largely amorphous structure with sporadic nanocrystals. FT-IR spectrum of Ar-U-CoFe PBA in Fig. 2(b) sees the disappearance of the band at around 1412 cm^{-1}, indicating the release of NH_4^+ during heat treatment. The comparison of FT-IR spectra of various Ar-U-CoFe PBA T °C (T = 200, 300, 600) (Fig. S8b) indicates that the release of NH_4^+ happens at 200–300 °C. Ar-U-CoFe PBA 300 °C maintains the crystalline structure, however, Ar-U-CoFe PBA 600 °C displays a completely different XRD pattern from PBA and deformed morphology (Fig. S8d and Fig. S9b). 400 °C is selected as an optimal temperature with moderate deformation. EDS mapping of Ar-U-CoFe PBA 400 °C (simplified as Ar-U-CoFe PBA unless otherwise stated) (Fig. S10) shows the homogeneous dispersion of Co, Fe, N, and C in a single cube, while the atomic ratio of Co, Fe, and N is around 1:0.8:3.9, with a higher N content than in Ar-CoFe PBA (Co:Fe:N = 1:0.8:2.8) (Fig. S11 and S7a). The broad band at around 1850–2240 cm^{-1} in the FT-IR spectrum of Ar-U-CoFe PBA contains four peaks (Fig. 2b), which are assigned to the stretching vibration of the remaining disordered Fe^{II}-CN-Co and Fe^{III}-CN-Co [24,38]. Besides, there is only one peak in the N 1s spectra of Ar-U-CoFe PBA at around 398.1 eV, originating from cyanide groups (Fig. S12), further confirming the removal of NH_4^+ [39,40]. Without the filling species in the interstitial space of the metal-cyanide framework, heat treatment process at 400 °C in Ar atmosphere on U-CoFe PBA can cause the collapse of its crystalline structure and lead to the amorphous characteristic of Ar-U-CoFe PBA after removing CN groups from lots of Fe-CN-Co units. The d-spacings of these clear lattice fringes in Ar-U-CoFe PBA are 0.494 and 0.248 nm, which well match with planes (2 0 0) and (4 0 0) of cubic CoFe PBA, respectively. The reduction of their d-spacing is attributed to the rearrangement of Fe-CN-Co units and the lack of fillings in the interstitial space. Besides, heat treatment process at 400 °C also removes the coordinated H_2O in U-CoFe PBA. These reactions could create a lot of edges and defects in the cube. In conclusion, Ar-U-CoFe PBA is a composite of disordered Fe-CN-Co units and PBA nanocrystals, as illustrated in Fig. 2(d).

3.1.5. Chemical valence states of Co and Fe

Chemical valence states of Co and Fe of the four samples are further investigated by XPS. Fe 2p and Co 2p high-resolution XPS spectra of CoFe PBA and U-CoFe PBA are similar in shape and position of the peaks. Two peaks at 708.5 and 721.3 eV of CoFe PBA and U-CoFe PBA in Fig. 3(a) are ascribed to Fe^{II} $2p_{3/2}$ and Fe^{II} $2p_{1/2}$, respectively. In Fig. 3(b), two doublets, corresponding to Co^{2+} $2p_{3/2}$ and Co^{2+} $2p_{1/2}$ at around 780.8 and 796.4 eV, respectively, and Co^{3+} $2p_{3/2}$ and Co^{3+} $2p_{1/2}$ at 782.4 and 797.6 eV, respectively, can be observed for both CoFe PBA and U-CoFe PBA. Charge transfer happens from the antibonding e_g^* orbital of Co^{2+} to the bonding t_{2g} orbital of Fe^{III} to maximize the ligand field stabilization energy, while the CoFe PBA is prepared with $K_3[Fe(CN)_6]_{(III)}$ and Co^{2+} [5,41,42]. The hydrothermal process does not alter the chemical state of Fe and Co. Therefore, the shared band at around 2087 cm^{-1} on FT-IR spectra of CoFe PBA and U-CoFe PBA originates from Fe^{II}-CN-$Co^{2+/3+}$ units. Chemical valences of Fe and Co in the two heat-treatment derivatives Ar-CoFe PBA and Ar-U-CoFe PBA are different from their precursors. The high-resolution spectra of Fe 2p of Ar-CoFe PBA and Ar-U-CoFe PBA exhibit peaks representing Fe^{II} (708.4 and 721.2 eV) and Fe^{III} (710.8 and 723.6 eV) (Fig. 3a), respectively. Besides this, a larger portion of Fe on the surface of Ar-U-CoFe PBA exhibits a higher chemical valence (Fe^{III} = 68 at%) compared to Ar-CoFe PBA (Fe^{III} = 37 at%) (Fig. S13a), which is believed to be beneficial to the OER performance [43]. There are two spin–orbit peaks at 781.7 and 796.9 eV in the high-resolution Co 2p XPS spectra of Ar-CoFe PBA and Ar-U-CoFe PBA (Fig. 3b), representing a mixed oxidation state of Co^{2+} and Co^{3+}, similar to previously reported Co 2p XPS spectra of Co_3O_4 [44–47]. The changes in the chemical states of Fe and Co are due to a thermally activated charge transfer along with the Fe-CN-Co linkage, which usually occurs in CoFe PBAs containing alkaline ions in the lattice [4,48]. One additional peak in the Co 2p XPS spectrum of Ar-CoFe PBA at 778.3 eV (Fig. 3 and Fig. S13b) is assigned to metallic Co in the cobalt-rich CoFe alloy nanoparticles on the surface. These results are consistent with the above discussion on samples' composition.

3.2. OER performance and analysis

3.2.1. OER activity

Electrocatalytic OER performance of CoFe PBA, U-CoFe PBA, Ar-CoFe PBA, and Ar-U-CoFe PBA is initially evaluated in 1.0 M KOH at room temperature with a standard three-electrode setup. The catalyst loading is optimized with a medium loading of 0.2 mg cm^{-2} displaying the best performance (Fig. S14), which is adopted for all the remaining tests on the RDE. Fig. 4(a) presents the iR-corrected

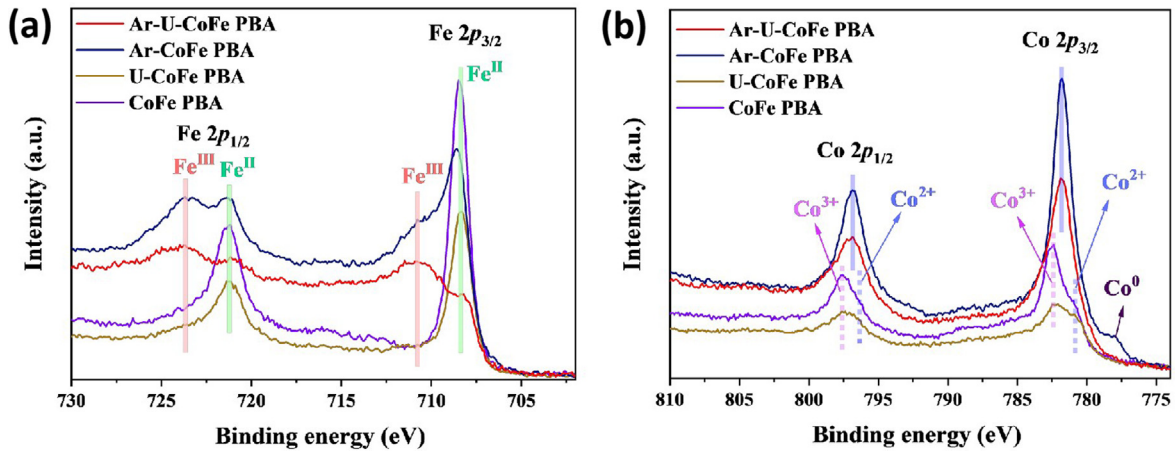

Fig. 3. Chemical states of Fe and Co. High-resolution XPS spectra of Fe 2*p* (a) and Co 2*p* (b) of CoFe PBA, U-CoFe PBA, Ar-CoFe PBA, and Ar-U-CoFe PBA.

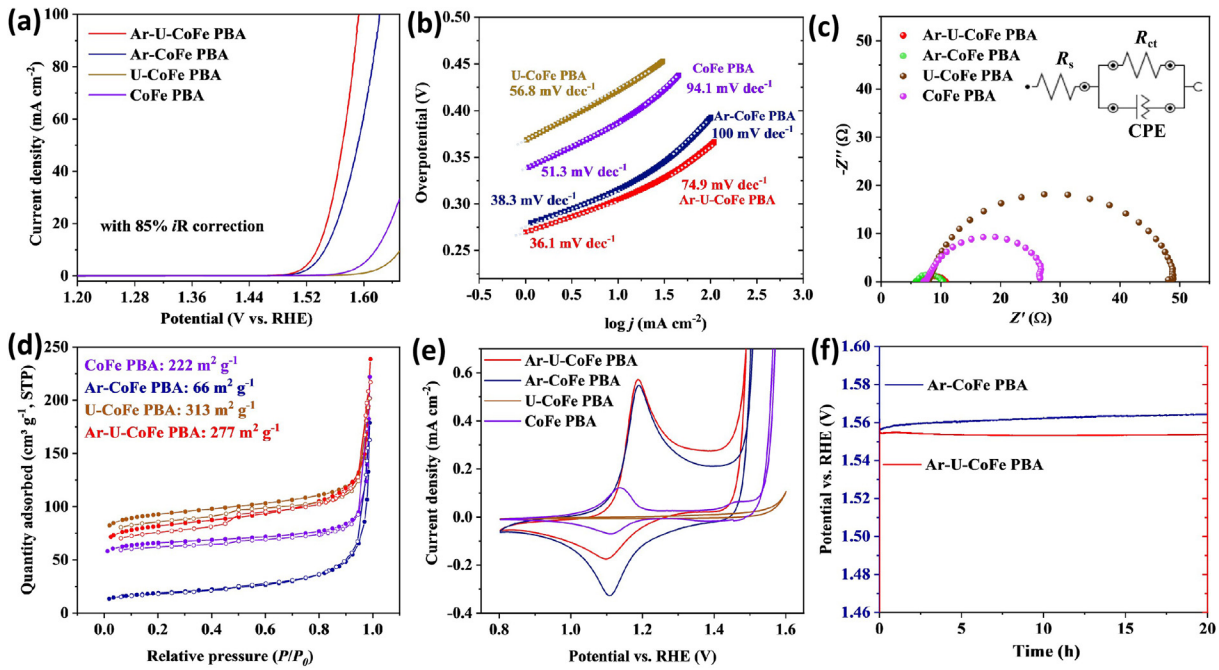

Fig. 4. OER performance evaluation. OER performance in 1.0 M KOH electrolyte using three-electrode system. (a) *i*R-corrected LSV curves and (b) corresponding Tafel plots of CoFe PBA, U-CoFe PBA, Ar-CoFe PBA, and Ar-U-CoFe PBA at room temperature. (c) Nyquist plots of CoFe PBA, U-CoFe PBA, Ar-CoFe PBA, and Ar-U-CoFe PBA, recorded at 1.60 V vs RHE. Inset is the equivalent circuit model used for fitting the EIS results. (d) Nitrogen adsorption (dot) - desorption (circle) isotherms of CoFe PBA, U-CoFe PBA, Ar-CoFe PBA, and Ar-U-CoFe PBA. (e) CV curves of CoFe PBA, U-CoFe PBA, Ar-CoFe PBA, Ar-U-CoFe PBA performed in the potential range of 0.80–1.60 V vs RHE at 5 mV s^{-1}. (f) Stability test at 10 mA cm^{-2} of Ar-CoFe PBA and Ar-U-CoFe PBA on RDE for 20 h at room temperature.

(85% *i*R compensation) LSV curves. Ar-U-CoFe PBA exhibits the best OER performance among the four samples with the smallest onset potential of ~ 1.46 V and a fast current rise with the applied potential. Ar-U-CoFe PBA requires overpotentials (η) of 270 and 305 mV to obtain 1 and 10 mA cm^{-2}, respectively, 280 and 316 mV for Ar-CoFe PBA, whereas 369 and 422 mV for U-CoFe PBA, 339 and 387 mV for CoFe PBA, 405 and 477 mV for carbon black only (Fig. S16), separately. In comparison to their derivatives, U-CoFe PBA and CoFe PBA, requiring much higher overpotentials to deliver the same current densities, are not active for electrocatalytic OER in alkaline condition. Comparison of the OER performance of Ar-U-CoFe PBA T °C (T = 300, 400, and 600) is shown in Fig. S15, with Ar-U-CoFe PBA 400 °C registering the highest current density at the same applied potential. The OER activity of Ar-U-CoFe PBA and Ar-CoFe PBA is comparable with other reported catalysts, such as porous CoFe PBA nanocubes fabricated by calcinating CoFe PBA in N_2 at 200 °C for 1 h (η_{10} = 316 mV) [49], FeCo oxide derived from CoFe PBA ($Co_3[Fe(CN)_6]_2$, η_{10} = 310 mV) [50], and other electrocatalysts listed in Table S1.

The OER pathway in alkaline electrolytes is generally described as the following reaction steps [43,51].

$M + OH^- \rightleftharpoons MOH + e^-$	Step1
$MOH + OH^- \rightleftharpoons MO + H_2O + e^-$	Step2
$MO + OH^- \rightleftharpoons MOOH + e^-$	Step3
$MOOH + OH^- \rightleftharpoons MOO^- + H_2O$	Step4
$MOO^- \rightleftharpoons M + O_2 + e^-$	Step5

M represents the active sites. In step 1, an OH^- is adsorbed on the active site (M), forming MOH with one-electron oxidation. MOH reacts with another OH^-, resulting in MO (step 2). In steps 3 and 4 , MO continues being oxidized to MOOH and MOO^-, following by O_2 desorption (step 5). The reaction rate of OER is influenced by multiple reaction steps including continuing OH^- adsorption, O—H bond breaking, and O_2 desorption. Tafel plots are profiled by plotting the overpotential (η) vs log current density (j) to analyze the OER kinetics. Tafel slope (b) can be determined by linear fitting of the Tafel plot ($\eta = a + b \times \log j$). The measured Tafel slopes can be used to analyze the possible rate-determining step (RDS) [43,52,53]. As shown in Fig. 4(b), Tafel plots mainly consist of two regions of different Tafel slopes, with one around 40 mV dec^{-1} at the low overpotential and the other one at the high overpotential tending to be higher to about 100 mV dec^{-1}. Based on the case study proposed by Shinagawa et al., we speculate that Step 5 is likely to be the RDS for OER. Besides, a small Tafel slope implies a favourable surface structure and composition for OER, which indicates that the intermediate forming at the early steps remains fast [43]. Ar-U-CoFe PBA possesses a smaller Tafel slope (36.1 mV dec^{-1}) than those of Ar-CoFe PBA (38.3 mV dec^{-1}), CoFe PBA (51.3 mV dec^{-1}), and U-CoFe PBA (56.8 mV dec^{-1}) at the low overpotential range. The Tafel slopes of Ar-U-CoFe PBA, Ar-CoFe PBA and CoFe PBA increase to 74.9, 100 and 94.1 mV dec^{-1}, respectively, at the high overpotential range up to 0.45 V. Therefore, Ar-U-CoFe PBA shows considerable OER kinetics.

EIS is an important characterization method to explore the electrochemical resistance during OER. Fig. 4(c) displays Nyquist plots of the four samples, which are simulated by the proposed equivalent circuit as inserted in the figure. Nyquist plots of Ar-U-CoFe PBA (3.8 Ω) and Ar-CoFe PBA (4.5 Ω) show visibly smaller semi-circular diameters, which represents charge-transfer resistance (R_{ct}) at the electrode–electrolyte interface, in contrast to those of U-CoFe PBA (41.0 Ω) and CoFe PBA (19.6 Ω) (Table S2). Overall, Ar-U-CoFe PBA possesses the smallest Tafel slope and fastest charge-transfer process among the four samples, which is consistent to its best OER performance among all the samples.

Electrochemical active surface area (ECSA) of the electrode is commonly evaluated by the double-layer capacitance (C_{dl}) calculated from CV curves performed at different current densities in the non-faradaic potential region (Figs. S17 and S18) [54]. However, we find that C_{dl}, in our case, does not necessarily correlate with the OER performance of the four materials due to their considerable distinctions with regard to chemical states and ion absorption in solution. Instead, we find a good correlation between the BET measured specific surface area and the OER performance (Fig. 4d). The specific surface area of U-CoFe PBA is around 313 m^2 g^{-1}, which is 81 m^2 g^{-1} larger than that of CoFe PBA (222 m^2 g^{-1}). This is likely due to the limited surface etching during the hydrothermal procedure. After heat treatment, the specific surface area of Ar-CoFe PBA decreases remarkably to ~ 66 m^2 g^{-1}, which could be explained by the growth of alloy nanoparticles and the aggregation of cubes. The specific surface area of Ar-U-CoFe PBA (277 m^2 g^{-1}) is slightly less than that of U-CoFe PBA (313 m^2 g^{-1}), and much larger than that of Ar-CoFe PBA, implying the different structural evolution during heat treatment leading to less aggregation. A large surface area, usually regarded as an advantage for catalysis, provides more active sites for the reaction [55,56].

Fig. 4(e) displays CV curves in a potential window of 0.80–1.60 V, showing the pre-oxidation/reduction behaviour of electrocatalysts (scan rate: 5 mV s^{-1}), which is believed to reflect the OER performance [15,57,58]. CoFe PBA exhibits two pairs of peaks at ~1.137/1.110 V (midpoint redox potential ($E_{1/2}$): 1.124 V; peak separation: 27 mV) and ~1.460/1.453 V ($E_{1/2}$: 1.457 V; peak separation: 7 mV), originating from the redox reaction of a high spin system $Co^{2+/3+}$ and the low spin $Fe^{II}(CN)_6^{4-}/Fe^{III}(CN)_6^{3-}$, respectively [59]. In the same potential window, U-CoFe PBA displays only a pair of peaks at ~1.327/1.268 V ($E_{1/2}$: 1.298 V, but with a larger peak separation (ΔE_p) of 59 mV) at 5 mV s^{-1} (Fig. S19). The poor redox behaviour of U-CoFe PBA is believed to be caused by the NH_4^+ node in interstitial sites, requiring higher energy to pass through the channels in comparison to that of K^+ in CoFe PBA's structure [60]. Ar-CoFe PBA has a pair of redox peaks at ~1.189/1.108 V ($E_{1/2}$: 1.149 V, 25 mV higher than that of CoFe PBA; ΔE_p: 81 mV), regarded as the joint redox wave of the Co and Fe species in the CoFe alloys nanoparticles. CV of Ar-U-CoFe PBA shows a similar characteristic with Ar-CoFe PBA with a pair of redox peaks at ~1.188/1.098 V ($E_{1/2}$: 1.143 V; ΔE_p: 90 mV). The redox peaks in the four samples' CV curves are in good agreement with chemical states of Co and Fe by XPS analysis.

Based on the above results and analysis, the improved OER performance of Ar-U-CoFe and Ar-CoFe PBA is very likely due to the chemical state change of Co and Fe during heat treatment. The metal species in Fe-CN-Co units are inert in OER due to the strong coordination with CN groups. Heat treatment efficiently causes the removal of partial CN groups and thus the reorganization of the material, liberating CoFe alloy nanoparticles in Ar-CoFe PBA and causing an amorphous structure with a large amount of unsaturated-coordinated Co and Fe atoms in Ar-U-CoFe PBA, which are more active for OER. Therefore, Ar-CoFe PBA and Ar-U-CoFe PBA require lower overpotentials and show smaller Tafel slopes and R_{ct} values than CoFe PBA and U-CoFe PBA.

3.2.2. OER stability

The long-term operational stability of Ar-U-CoFe PBA and Ar-CoFe PBA is characterized by CP method (Fig. 4f). Ar-U-CoFe PBA shows excellent stability at 10 mA cm^{-2} without visible potential shift for 20 h. The overpotential required by Ar-CoFe PBA at the same condition exhibits a slight increase of ~7 mV. The LSV curves of Ar-CoFe PBA and Ar-U-CoFe PBA after stability test (Fig. S20) further indicates the slight overpotential increase. Samples pasted on the Ni foam exhibit a similar trend during a 40 h CP test (Fig. S21). Fig. 5(a) shows that the long-term OER test destroyed the cubic structure of Ar-CoFe PBA greatly, which turned into typical transition metals (like Ni, Fe, and Co) (oxy)hydroxides' layered structure [61,62]. In sharp contrast, Ar-U-CoFe PBA remains its initial cubic shape after the long-term OER test, as indicated in Fig. 5(d). The layered structure of metal (oxy)hydroxides, smaller than those from Ar-CoFe PBA, can also be observed at the outmost of the cube (Fig. 5b and e). HRTEM images of both samples after a long-term test (Fig. 5c and f) show some spots with a lattice fringe spacing determined to be 0.297 nm, which can be ascribed to the (2 2 0) plane of CoFe oxide (ICSD Coll. Code of 17714). Elemental chemical states analysis of Ar-U-CoFe PBA and Ar-CoFe PBA after 40 h stability test by XPS is displayed in Fig. S22. High-resolution XPS spectra of Fe 2*p* and Co 2*p* of these 2 samples (Fig. S22a and b) exhibit similar shapes and both contain Co^{2+}, Co^{3+}, Fe^{2+}, and Fe^{3+}, indicative of the similar chemical environment of Co and Fe on the surface. High-resolution XPS spectra of O 1*s* (Fig. S22c) are composed of three peaks attributed to M−O, M−OH, and absorbed water (M represents Co and Fe), respectively. Based on the TEM and XPS analysis, the surface of Ar-CoFe PBA and Ar-U-CoFe PBA is converted to CoFe (oxy)hydroxides and oxides during continuous OER [26,63]. Besides, both XPS (Fig. S22) and EDS (Fig. S23) indicate that there is no element N on the surface and lots of Co and Fe, indicative of the complete dissolution of CN groups and suppressed leaching of Fe during the stability test. These phenomena are common and reported when using PBAs as OER catalysts [23,64]. Ar-U-CoFe PBA presenting better stability than Ar-CoFe PBA is largely attributed to its amorphous structure and enriched defects after

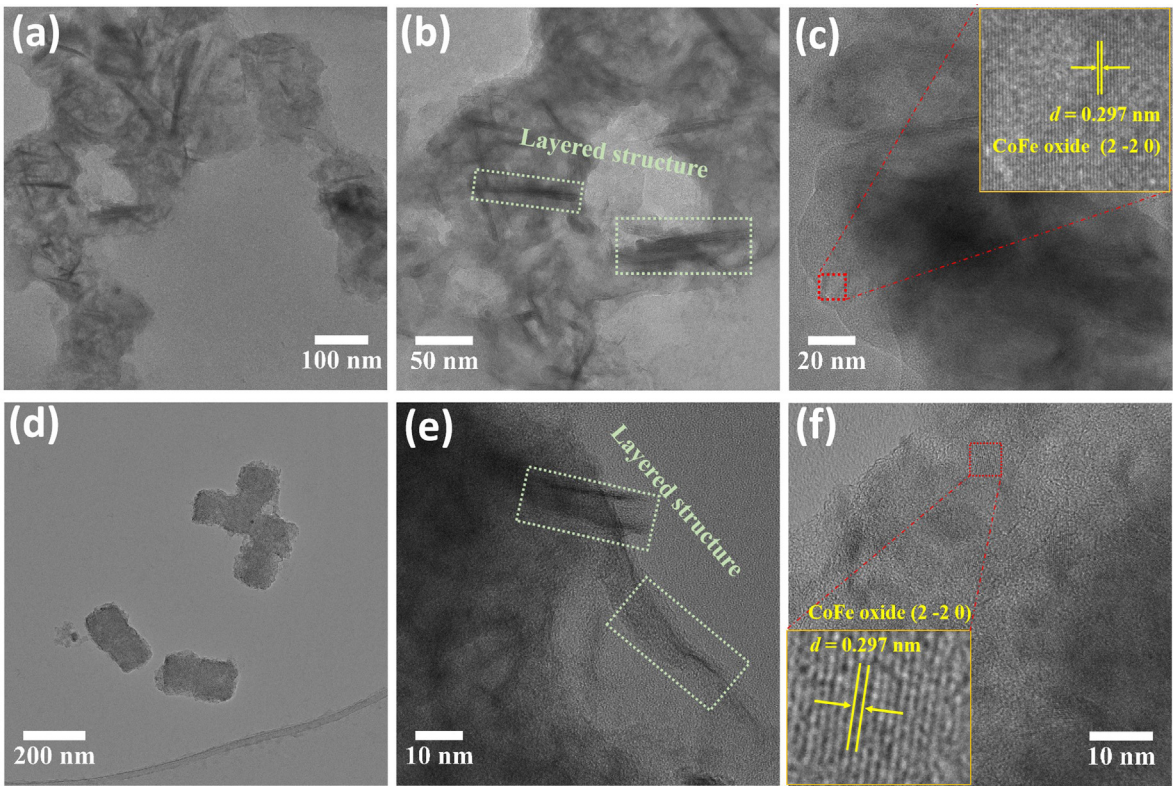

Fig. 5. Sample characterization after stability test. TEM and HRTEM images of Ar-CoFe PBA after 40 h OER stability test (a–c) and Ar-U-CoFe PBA (d–f) after 40 h OER stability test. Inset of (c) and (f) are the magnified HRTEM images of the corresponding samples.

heat treatment. In other words, a large amount of disordered Fe-CN-Co units and PBA nanoparticles in Ar-U-CoFe PBA hamper the morphology's acute transformation and provide superior stability.

Finally, a single-cell electrolyzer is assembled as Fig. 6(a), with Ar-U-CoFe PBA sprayed on Ni foam as the anode and a Pt/C based cathode. The electrolyzer requires a cell voltage of 1.66 V to

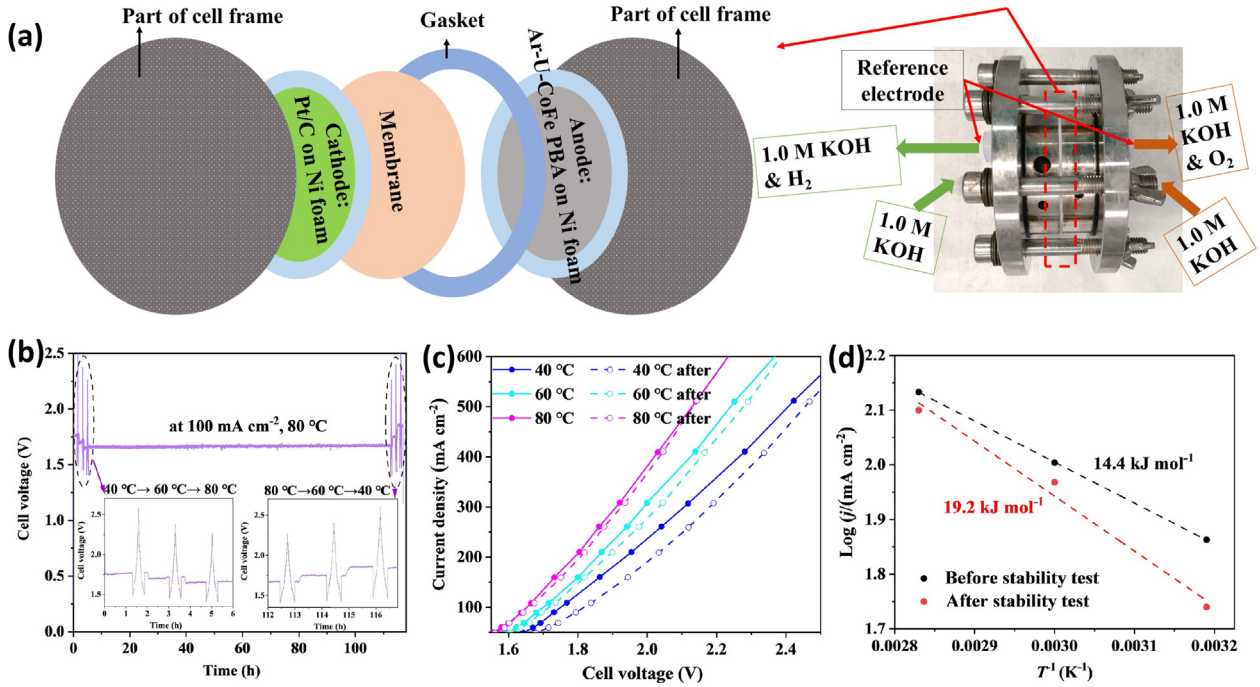

Fig. 6. Performance evaluation of Ar-U-CoFe PBA as the anode of an alkaline electrolyzer. (a) Cartoon and the digital photo of the alkaline electrolyzer used for the two-electrode test. (b) Chronopotentiometry (CP) test of the electrolyzer at 100 mA cm^{-2} and 80 °C for about 100 h. The noises at the start and end are due to the polarization curves testing. (c) Polarization curves at 40, 60, and 80 °C before (dot) and after (circle) the CP stability test in a course of about 100 h. (d) The corresponding Arrhenius plots at the cell voltage of 1.70 V based on the polarization curves in (c).

achieve 100 mA cm^{-2} at 80 °C and exhibits excellent stability with a negligible cell voltage increase of ~0.01 V after the 100 h test (Fig. 6b). At 40 and 60 °C, it needs higher initial cell voltages of 1.76 and 1.70 V, respectively, to deliver 100 mA cm^{-2}, separately requiring higher cell voltage increases of 0.09 and 0.05 V after the stability test as shown in Fig. 6(c). The apparent activation energy of OER for a catalyst can be determined by the Arrhenius plot: $\log(j) = -0.434E_a/(RT) + \text{const}$, where R represents the Boltzmann constant (8.315 J g^{-1} mol^{-1} K^{-1}) and E_a is the activation energy (J g^{-1} mol^{-1}) [65,66]. Based on derived Arrhenius plots at the cell voltage of 1.70 V (Fig. 6d), the initial E_a is 14.4 kJ mol^{-1}, which slightly increases to 19.2 kJ mol^{-1} after the stability test, further indicating good activity and stability of Ar-U-CoFe PBA towards OER. Note that the E_a obtained here is from a full electrolyzer, and such values are comparable to other reported OER catalysts like FeCoW oxyhydroxides (49 kJ mol^{-1}), CoO_x (11.1 kJ mol^{-1}), and $NiFeO_x$ (25 kJ mol^{-1}) [65–67].

4. Conclusions

Overall, we have explored the composition, crystalline structure, and morphology of CoFe PBA, U-CoFe PBA, and their derivatives Ar-CoFe PBA, and Ar-U-CoFe PBA. It is confirmed by various characterization techniques (FT-IR, XPS, EDS, TGA, XRD, and HRTEM) that K^+ in the interstitial space can be completely replaced by NH_4^+ without destroying the cubic morphology and changing the chemical state of Fe and Co by a hydrothermal procedure in the aqueous urea solution. Heat treatment of PBAs at high temperatures (200–600 °C) in an Ar atmosphere can remove H_2O, NH_4^+, and CN groups, and change materials' phase and composition. 400 °C is a moderate heat-treatment temperature. CoFe alloy nanoparticles grow on the surface of CoFe PBA, while U-CoFe PBA's framework collapses and becomes amorphous with PBA nanocrystals. Electrochemical OER performance of these four samples in alkaline solution varies, showing that heat-treatment derivatives behave favourably over the pristine PBAs due to the moderated composition and chemical environment and states of Co and Fe in Ar-CoFe PBA and Ar-U-CoFe PBA. Ar-U-CoFe PBA (η_{10} = 305 mV, Tafel slope = 36.1 mV dec^{-1}) outperforms Ar-CoFe PBA (η_{10} = 316 mV, Tafel slope = 38.3 mV dec^{-1}) in terms of electrochemical activity and operational stability, exhibiting a promising anode material in an assembled alkaline electrolyzer, beneficial from the amorphous structure embedded with tiny PBA crystals. This work is meaningful to the development of new PBAs and derivatives and their application in the electrocatalysis of water oxidation.

Declaration of competing interest

The authors declare that they have no known competing financial interests or personal relationships that could have appeared to influence the work reported in this paper.

Acknowledgments

Financial support from the China Scholarship Council (201806220068, 201806650009) to F.D. and X.Y., and the Villum Experiment (grant No. 35844) to X.X. is greatly acknowledged. Kai Gao at DTU Kemi is sincerely acknowledged for the collection and analysis of TGA data. Prof. Qingfeng Li at DTU Energy is thanked for the great help on the project.

Appendix A. Supplementary material

Supporting information is available for this manuscript, which includes supplementary SEM images, XRD patterns, FT-IR spectra, and XPS spectra of samples mentioned in this work; supplementary electrochemical polarization curves; electrochemical-double-layer capacitance measurement in non-OER region; post-test characterization; supplementary summarizing tables.

Supplementary data to this article can be found online at https://doi.org/10.1016/j.jechem.2022.11.050.

References

[1] Y. Moritomo, H. Tanaka, Adv. Condens. Matter Phys. 2013 (2013).
[2] J. Lejeune, J.B. Brubach, P. Roy, A. Bleuzen, Comptes Rendus Chim. 17 (2014) 534–540.
[3] H. Yi, R. Qin, S. Ding, Y. Wang, S. Li, Q. Zhao, F. Pan, Adv. Funct. Mater. 31 (2021) 2006970.
[4] J.D. Cafun, G. Champion, M.A. Arrio, C.C. Dit Moulin, A. Bleuzen, J. Am. Chem. Soc. 132 (2010) 11552–11559.
[5] A. Bleuzen, C. Lomenech, V. Escax, F. Villain, F. Varret, Cartier, C. Moulin, M. Verdaguer, J. Am. Chem. Soc. 122 (2000) 6648–6652.
[6] L. Jiang, Y. Lu, C. Zhao, L. Liu, J. Zhang, Q. Zhang, X. Shen, J. Zhao, X. Yu, H. Li, X. Huang, L. Chen, Y.S. Hu, Nat. Energy. 4 (2019) 495–503.
[7] X. Wu, Y. Xu, H. Jiang, Z. Wei, J.J. Hong, A.S. Hernandez, F. Du, X. Ji, ACS Appl. Energy Mater. 1 (2018) 3077–3083.
[8] X. Wu, Y. Qi, J.J. Hong, Z. Li, A.S. Hernandez, X. Ji, Angew. Chemie. 129 (2017) 13206–13210.
[9] P. Bhatt, S. Banerjee, S. Anwar, M.D. Mukadam, S.S. Meena, S.M. Yusuf, ACS Appl. Mater. Interfaces. 6 (2014) 17579–17588.
[10] M.R. Hartman, V.K. Peterson, Y. Liu, S.S. Kaye, J.R. Long, Chem. Mater. 18 (2006) 3221–3224.
[11] P.K. Thallapally, R.K. Motkuri, C.A. Fernandez, B.P. McGrail, G.S. Behrooz, Inorg. Chem. 49 (2010) 4909–4915.
[12] A. Takahashi, H. Tanaka, D. Parajuli, T. Nakamura, K. Minami, Y. Sugiyama, Y. Hakuta, S.I. Ohkoshi, T. Kawamoto, J. Am. Chem. Soc. 138 (2016) 6376–6379.
[13] L.M. Cao, D. Lu, D.C. Zhong, T.B. Lu, Coord. Chem. Rev. 407 (2020).
[14] F. Diao, W. Huang, G. Ctistis, H. Wackerbarth, Y. Yang, P. Si, J. Zhang, X. Xiao, C. Engelbrekt, ACS Appl. Mater. Interfaces. 13 (2021) 23702–23713.
[15] J.H. Lee, S. Kattel, Y. Wang, B.M. Tackett, Z. Xie, S. Hwang, S.R. Denny, W. Xu, J. G. Chen, J. Catal. 393 (2021) 390–398.
[16] L. Han, P. Tang, Á. Reyes-Carmona, B. Rodríguez-García, M. Torréns, J.R. Morante, J. Arbiol, J.R. Galan-Mascaros, J. Am. Chem. Soc. 138 (2016) 16037–16045.
[17] Y. Zeng, G.F. Chen, Z. Jiang, L.X. Ding, S. Wang, H. Wang, J. Mater. Chem. A. 6 (2018) 15942–15946.
[18] S.H. Kwag, Y.S. Lee, J. Lee, D.I. Jeong, S. Bin Kwon, J.H. Yoo, S. Woo, B.S. Lim, W.K. Park, M.J. Kim, J.H. Kim, B. Lim, B.K. Kang, W.S. Yang, D.H. Yoon, ACS Appl. Energy Mater. 2 (2019) 8502–8510.
[19] B.K. Kang, S.Y. Im, J. Lee, S.H. Kwag, S. Bin Kwon, S.N. Tiruneh, M.J. Kim, J.H. Kim, W.S. Yang, B. Lim, D.H. Yoon, Nano Res. 12 (2019) 1605–1611.
[20] M. Hu, S. Ishihara, K. Ariga, M. Imura, Y. Yamauchi, Chem. - A Eur. J. 19 (2013) 1882–1885.
[21] X. Zhang, M. Xia, T. Liu, N. Peng, H. Yu, R. Zheng, L. Zhang, M. Shui, J. Shu, Chem. Eng. J. 421 (2021).
[22] K. Zhang, T.H. Lee, J.H. Cha, R.S. Varma, J.W. Choi, H.W. Jang, M. Shokouhimehr, ACS Omega. 4 (2019) 21410–21416.
[23] Z.Y. Yu, Y. Duan, J.D. Liu, Y. Chen, X.K. Liu, W. Liu, T. Ma, Y. Li, X.S. Zheng, T. Yao, M.R. Gao, J.F. Zhu, B.J. Ye, S.H. Yu, Nat. Commun. 10 (2019) 2799.
[24] J. Coates, Encycl, Anal. Chem. (2006), https://doi.org/10.1002/9780470027318.a5606.
[25] Q. Wang, N. Wang, S. He, J. Zhao, J. Fang, W. Shen, Dalt. Trans. 44 (2015) 12878–12883.
[26] G. Zhang, Y. Li, X. Xiao, Y. Shan, Y. Bai, H.G. Xue, H. Pang, Z. Tian, Q. Xu, Nano Lett. 21 (2021) 3016–3025.
[27] P. Bhatt, S.S. Meena, M.D. Mukadam, B.P. Mandal, A.K. Chauhan, S.M. Yusuf, New J. Chem. 42 (2018) 4567–4578.
[28] M. Manivannan, S. Rajendran, Int. J. Eng. Sci. Tech. 3 (2011) 8048–8060.
[29] C.G. Barreras-Urbina, M. Plascencia-Jatomea, F.J. Wong-Corral, M. Pérez-Tello, A.I. Ledesma-Osuna, J.A. Tapia-Hernández, D.D. Castro-Enríquez, E.O. Rueda-Puente, F. Rodríguez-Félix, Polym. Bull. 77 (2020) 6525–6541.
[30] Y. Jiang, A. Takahashi, T. Kawamoto, M. Asai, N. Zhang, Z. Lei, Z. Zhang, K. Kojima, K. Imoto, K. Nakagawa, S.I. Ohkoshi, T. Nakamura, Chem. Commun. 54 (2018) (1964) 11961–11971.
[31] Y. Song, Q. Pan, H. Lv, D. Yang, Z. Qin, M.Y. Zhang, X. Sun, X.X. Liu, Angew. Chemie - Int. Ed. 60 (2021) 5718–5722.
[32] S. Petit, D. Righi, J. Madejová, Appl. Clay Sci. 34 (2006) 22–30.
[33] M. Loukil, A. Ben Salah, A. Kabadou, J. Alloys Compd. 488 (2009) L10–L13.
[34] Y. Soni, I. Kavya, T.G. Ajithkumar, C.P. Vinod, Chem. Commun. 54 (2018) 12412–12415.
[35] K. Shimizu, A. Shchukarev, J.F. Boily, J. Phys. Chem. C. 115 (2011) 6796–6801.

[36] Y. Guo, T. Wang, J. Chen, J. Zheng, X. Li, K. Ostrikov (Ken), Adv. Energy Mater. 8 (2018) 1800085.
[37] O. Sato, Y. Einaga, A. Fujishima, K. Hashimoto, Inorg. Chem. 38 (1999) 4405–4412.
[38] A. Winston, R.N. Kemper, Tetrahedron 27 (1971) 543–548.
[39] C. Gu, L. Yang, M. Wang, N. Zhou, L. He, Z. Zhang, M. Du, Microchim. Acta. 186 (2019) 343.
[40] K. Siuzdak, M. Szkoda, J. Karczewski, J. Ryl, A. Lisowska-Oleksiak, RSC Adv. 6 (2016) 76246–76250.
[41] F.S. Hegner, J.R. Galán-Mascarós, N. López, Inorg. Chem. 55 (2016) 12851–12862.
[42] C. Cartier Dit Moulin, F. Villain, A. Bleuzen, M.A. Arrio, P. Sainctavit, C. Lomenech, V. Escax, F. Baudelet, E. Dartyge, J.J. Gallet, M. Verdaguer, J. Am. Chem. Soc. 122 (2000) 6653–6658.
[43] T. Shinagawa, A.T. Garcia-Esparza, K. Takanabe, Sci. Rep. 5 (2015) 13801.
[44] S. Kalasina, N. Phattharasupakun, J. Wutthiprom, V. Promarak, T. Sudyoadsuk, M. Sawangphruk, ECS Trans. 85 (2018) 435–447.
[45] G. Liu, L. Ma, Q. Liu, Electrochim. Acta. 364 (2020).
[46] J. Si, S. Xiao, Y. Wang, L. Zhu, X. Xia, Z. Huang, Y. Gao, Nanoscale. 10 (2018) 2596–2602.
[47] J. Zhou, Q. Shen, J. Yang, M. Tariq, W. Sun, L. Cao, J. Yang, Environ. Sci. Pollut. Res. (2021) 65487–65498.
[48] D. Aguilà, Y. Prado, E.S. Koumousi, C. Mathonière, R. Clérac, R. Clérac, Chem. Soc. Rev. 45 (2016) 203–224.
[49] S. Jo, S. Noh, K.R. Wee, J.H. Shim, ChemElectroChem. 7 (2020) 3725–3732.
[50] C.H. Chuang, L.Y. Hsiao, M.H. Yeh, Y.C. Wang, S.C. Chang, L.D. Tsai, K.C. Ho, ACS Appl. Energy Mater. 3 (2020) 11752–11762.
[51] W. Huang, J. Tang, F. Diao, C. Engelbrekt, J. Ulstrup, X. Xiao, K. Mølhave, ChemElectroChem. 7 (2020) 4695–4712.
[52] L. Negahdar, F. Zeng, S. Palkovits, C. Broicher, R. Palkovits, ChemElectroChem. 6 (2019) 5588–5595.
[53] X. Xiao, C. Engelbrekt, Z. Li, P. Si, Electrochim. Acta. 173 (2015) 393–398.
[54] W. Huang, J. Tang, F. Diao, S. Li, H. Sun, X. Xiao, J. Electrochem. Soc. 168 (2021) 94501.
[55] W. Yang, S. Chen, Chem. Eng. J. 393 (2020).
[56] J. Mohammed-Ibrahim, J. Power Sources. 448 (2020).
[57] W. Huang, C. Peng, J. Tang, F. Diao, M. Nulati Yesibolati, H. Sun, C. Engelbrekt, J. Zhang, X. Xiao, K.S. Mølhave, J. Energy Chem. 65 (2021) 78–88.
[58] F. Ma, Q. Wu, M. Liu, L. Zheng, F. Tong, Z. Wang, P. Wang, Y. Liu, H. Cheng, Y. Dai, Z. Zheng, Y. Fan, B. Huang, ACS Appl. Mater. Interfaces. 13 (2021) 5142–5152.
[59] R. Koncki, Crit. Rev. Anal. Chem. 32 (2002) 79–96.
[60] S. Qiu, Y. Xu, X. Wu, X. Ji, Electrochem. Energy Rev. 5 (2022) 242–262.
[61] J. Hu, C. Zhang, L. Jiang, H. Lin, Y. An, D. Zhou, M.K.H. Leung, S. Yang, Joule. 1 (2017) 383–393.
[62] L. Yu, H. Zhou, J. Sun, F. Qin, D. Luo, L. Xie, F. Yu, J. Bao, Y. Li, Y. Yu, S. Chen, Z. Ren, Nano Energy. 41 (2017) 327–336.
[63] X. Xu, T. Wang, L. Su, Y. Zhang, L. Dong, X. Miao, A.C.S. Sustain Chem. Eng. 9 (2021) 5693–5704.
[64] X. Su, Y. Wang, J. Zhou, S. Gu, J. Li, S. Zhang, J. Am. Chem. Soc. 140 (2018) 11286–11292.
[65] E. Nurlaela, T. Shinagawa, M. Qureshi, D.S. Dhawale, K. Takanabe, ACS Catal. 6 (2016) 1713–1722.
[66] S. Xu, C. Lv, T. He, Z. Huang, C. Zhang, J. Mater. Chem. A. 7 (2019) 7526–7532.
[67] B. Zhang, X. Zheng, O. Voznyy, R. Comin, M. Bajdich, M. García-Melchor, L. Han, J. Xu, M. Liu, L. Zheng, F. Pelayo García de Arquer, C.T. Dinh, F. Fan, M. Yuan, E. Yassitepe, N. Chen, T. Regier, P. Liu, Y. Li, P. De Luna, A. Janmohamed, H.L. Xin, H. Yang, A. Vojvodic, E.H. Sargent, Science 352 (2016) 333–337.